Journal of Materials Chemistry A

ROYAL SOCIETY OF CHEMISTRY

PAPER

View Article Online
View Journal | View Issue

Cite this: J. Mater. Chem. A, 2025, 13, 5987

Multifunctional hydroxyurea additive enhances high stability and reversibility of zinc anodes†

Ruizhe Zhang, ‡[a] Zhiyong Liao, ‡[a] Yongbo Fan, *[b] Lixin Song, [a] Jiayi Li,[a] Zhuo Zhang,[a] Peizhi Dong, [a] Zexue Lin,[a] Ning Yang, [a] Qingfeng Zhang[c] and Huiqing Fan *[a]

The performance of aqueous zinc-ion batteries (AZIBs) is greatly influenced by both the electric double layer (EDL) at the Zn electrode/electrolyte interface and the solvation structure of Zn^{2+}. In this study, hydroxyurea (HU), a widely used and low-cost polar molecule in the medical field, is innovatively introduced as an additive to optimize both the EDL and the solvation structure of Zn^{2+}, thereby enhancing the stability and reversibility of the zinc anode. HU coordinates with Zn^{2+} through its polar functional groups, altering the solvation structure and reshaping the intrinsic hydrogen bonding network. Additionally, due to HU's strong adsorption capabilities, it forms a water-poor inner Helmholtz plane (IHP), effectively suppressing parasitic reactions and dendrite growth, while promoting uniform zinc deposition on the (002) crystal plane. The Zn//Zn symmetric cells with HU-modified electrolyte exhibit outstanding cycling stability, cycling over 2600 hours at 1 mA cm^{-2} at room temperature, and over 1700 hours at 1 mA cm^{-2} under low-temperature conditions (−25 °C). The Zn//MnO_2 full cell retains 86.88% of its initial capacity after 1400 cycles, with ultra-high coulombic efficiency (99.8%). Furthermore, the Zn//MnO_2 pouch cell assembled with HU-modified electrolyte demonstrates a high-capacity retention rate of 83.7% after 300 cycles, showing excellent commercial potential. These results indicate that as an effective additive, HU provides a promising route for high-performance and scalable AZIBs.

Received 26th December 2024
Accepted 21st January 2025

DOI: 10.1039/d4ta09186h

rsc.li/materials-a

1 Introduction

As environmental pollution worsens and natural resources deplete, the need for renewable energy to replace non-renewable energy sources has become urgent.[1] Aqueous batteries are among the most promising solutions due to their low cost, non-flammability, and environmental friendliness.[2] Notable for their low redox potential (−0.76 V *vs.* SHE), high theoretical capacity (820 mA h g^{-1}), and abundant availability in the Earth's crust,[3,4] aqueous zinc-ion batteries (AZIBs) have emerged as highly promising candidates among aqueous energy storage systems.[3] However, long-term cycling introduces several challenges, including electrolyte–Zn anode interactions, uncontrolled Zn dendrite growth, instability of the solid–liquid interface, and undesirable parasitic reactions.[5–8] These issues significantly hinder the cycle life, coulombic efficiency, and Zn plating/stripping reversibility, limiting the practical viability of AZIBs.[9]

Considerable research has been dedicated to addressing these challenges,[10] which can be broadly categorized into three strategies: anode alloying,[11,12] artificial interfacial coatings,[13–17] and electrolyte optimization. Among these strategies, electrolyte optimization stands out as a promising strategy for AZIBs commercialization, given its cost-effectiveness, simplicity, and proven efficacy. Common electrolyte optimization strategies include the "water-in-salt rlectrolyte (WISE)"[18] system and the addition of functional additives to existing electrolytes.[19] Liu and colleagues at the Shanghai Institute of Ceramics developed a high-concentration dual-salt electrolyte (HC-DSE), achieving a reduction in water activity and suppressing side reactions by tailoring the solvation structure with dual high-concentration salts.[20] Similarly, Wang and his team at the University of Maryland designed a supersaturated electrolyte utilizing $ZnCl_2$, $ZnBr_2$, and $Zn(OAc)_2$, forming an acetate-terminated salt-water oligomer and exceeding traditional solubility limits by raising the salt concentration to 75 M.[21] However, the high salt concentration significantly raises production costs, and the low viscosity and suboptimal conductivity in the WISE system limit Zn^{2+} diffusion kinetics, presenting major challenges to the commercial adoption of the water-in-salt approach.[10,22,23] Introducing a small amount of

[a]State Key Laboratory of Solidification Processing, School of Materials Science and Engineering, Northwestern Polytechnical University, Xi'an 710072, PR China. E-mail: hqfan@nwpu.edu.cn

[b]Department of Applied Physics, The Hong Kong Polytechnic University, Hung Hom 100872, Hong Kong, PR China

[c]Hubei Key Laboratory of Micro-Nanoelectronic Materials and Devices, School of Materials Science and Engineering, Hubei University, Wuhan 430062, PR China

† Electronic supplementary information (ESI) available. See DOI: https://doi.org/10.1039/d4ta09186h

‡ Ruizhe Zhang and Zhiyong Liao contributed equally to this work.

functional additives, therefore, has emerged as the most promising approach for optimizing Zn-ion battery performance.[24]

In conventional aqueous zinc-ion battery electrolytes, the strong electrostatic interaction between Zn^{2+} and H_2O molecules leads to the formation of a $[Zn(H_2O)_6]^{2+}$ solvation structure.[25] Upon discharge, hydrated Zn^{2+} are attracted and diffuse towards the anode surface, where they will release active free water molecules and participate in electrochemical or side reactions, leading to corrosion.[26] Notably, this reaction is confined within the electric double layer (EDL). Specifically, the inner layer of the EDL, known as the inner Helmholtz plane (IHP), is composed solely of densely packed water molecules. This layer strongly hinders the desolvation of hydrated Zn^{2+}, which exacerbates competing reactions such as the hydrogen evolution reaction (HER).[27,28] The second layer, known as the outer Helmholtz plane (OHP), is also called the residual charge layer, the ions in the outer charge layer do not directly contact the electrode surface like those in the IHP. Instead, they exist in a "diffused" form under the influence of the electric field, therefore, this layer has minimal influence on the electrochemical reactions of hydrated zinc ions.[29] During discharge, the hydrated zinc ions must dissociate from the water molecules in the EDL to undergo reduction. Furthermore, the hindered desolvation process, coupled with the strong repulsive forces within the IHP, leads to uneven deposition of zinc ions,[30] thereby inducing the formation of zinc dendrites.[31] Therefore, modifying the Zn^{2+} solvation structure and developing a poor-water-content EDL are regarded as essential steps in enhancing battery stability and performance.

In recent years, organic additives rich in functional groups have received significant interest, including tetramethylurea (TMU),[32] glucose (GLU),[33] *N*-methyl pyrrolidone (NMP),[34] and *N*,*N*-dimethylformamide (DMF),[35] and others. These functional additives contain hydrogen bond donor groups (–OH, $–NH_2$) and hydrogen bond acceptor groups (–C=O),[36] which disrupt the intrinsic hydrogen-bond network, modifying the coordination environment of Zn^{2+} and enhancing the coordination number of co-solvents.[32] Regrettably, these additives have limitations due to their narrow scope of control. Under conditions of deep cycling, intense hydrogen evolution reactions (HER) still occur;[37] Moreover, compared to laboratory-scale coin cells with capacities of only a few μA h, larger electrodes suffer severe parasitic reactions. When assembled into Ah-level pouch cells for high-capacity batteries, the interfacial stability further deteriorates.[38] L. Jiang *et al.* found that quaternary ammonium cations could occupy the IHP in the EDL, forming a low-water-content IHP that significantly suppresses HER.[26] Meanwhile, Xu *et al.* utilized the specific adsorption properties of trifluoroacetic acid ($–CF_3COOH$) and hydroxyl groups (–OH), which tightly adsorb onto the electrode surface, restructuring the EDL to further create a low-water-content double layer.[39] Based on this discussion, if a functional additive not only includes hydrogen bond donor/acceptor groups but also regulates intrinsic hydrogen bonding in the EDL to establish a poor-water-content EDL, it would present an excellent strategy for enhancing the stability of the Zn anode.

Herein, we selected hydroxyurea (HU), an inexpensive polar molecule widely used in the medical field, as a novel additive for zinc-ion batteries. HU not only reshapes the solvation structure of Zn^{2+} but also modifies the EDL structure. Fig. S1† shows the molecular formula of HU, where the high electron density amide group is connected to $–NH_2$ on one end and –OH on the other end. This gives HU multiple functional properties. Specifically, the polar functional groups in HU can form strong coordination with Zn^{2+}, disrupt the intrinsic hydrogen bond network between water molecules, and establish stronger hydrogen bonds with them. This transformation also converts bound water molecules into free water molecules (the activity of free water molecules in this part is relatively low[26]), driven by HU's strong affinity for both water and zinc ions. Both theoretical and experimental studies indicate that the coordination of Zn^{2+} shifts from the classic $[Zn(H_2O)_6]^{2+}$ to $[Zn(H_2O)_5(HU)]^{2+}$. Moreover, HU adsorbs tightly due to the specific adsorption of hydroxyl groups and the strong electrostatic interactions between the high electron density of the carbonyl groups and zinc. This adsorption displaces some water molecules and creates a water-poor IHP. The alteration of the IHP in the EDL guides Zn^{2+} to deposit preferentially at the (002) crystal plane during prolonged electroplating/stripping cycles, suppressing side reactions caused by bound water and inhibiting zinc dendrite growth (Fig. 1). In contrast, the control sample with 2 M $ZnSO_4$ (ZNS) electrolyte experiences uneven Zn^{2+} deposition, leading to rampant dendrite growth. Additionally, the unchanged dense hydrated IHP structure in the control sample allows for uninhibited HER at the electrode surface. As shown in Fig. S2,† HU's high solubility in water also enhances the reaction kinetics of Zn^{2+},[40] reflected in increased ion mobility and improved deposition behavior. Consequently, the Zn//Zn symmetric cell using HU-containing electrolyte demonstrated excellent cycling performance (1 mA, 0.5 mA h cm^{-2} for over 2600 hours), and achieved stable cycling for over 1700 hours under extreme low-temperature conditions while the Zn//Cu asymmetric battery cycled stably for over 1600 hours at a current density of 1 mA, 0.5 mA h cm^{-2}, with a high coulombic efficiency (CE) of 99.34%. Furthermore, the Zn//MnO_2 full cell exhibited remarkable performance, maintaining 86.88% of its capacity after more than 1400 cycles and achieving an ultra-high CE of over 99.8%. Although many urea-based compounds have been reported as additives for zinc-ion batteries, their regulatory effects have typically been limited to solvation structure modification and the construction of unstable SEI layers.[32,41] This study not only provides a detailed exploration of the role of HU molecules in Zn^{2+} solvation but also investigates their impact on EDL regulation, offering a novel perspective for future research.

2 Experimental

2.1 Preparations of electrolyte

Firstly, weigh the required amount of 4 × 2 M ZNS using an electronic balance and place it in a 4 × 5 mL glass bottle. Using a micropipette, measure the required amount of distilled water and add it to the glass bottle. Place the bottle on a magnetic

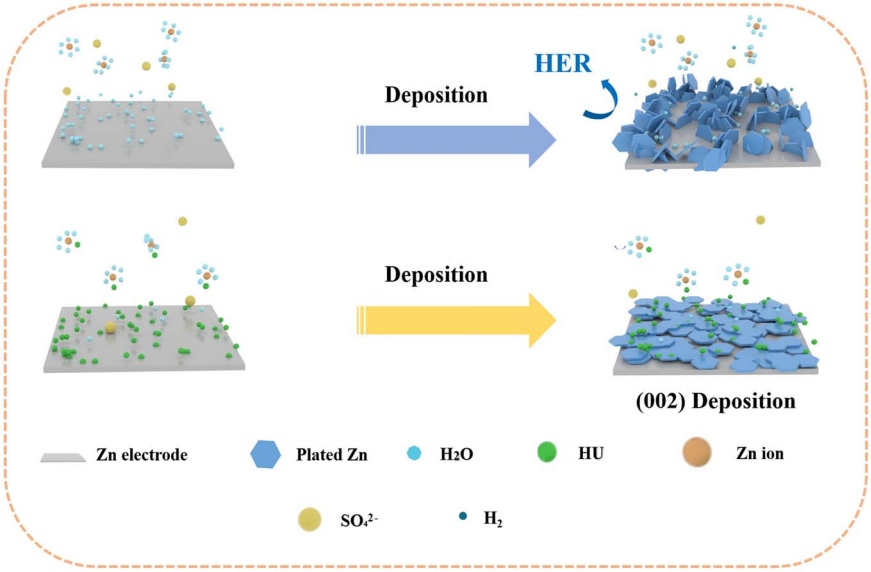

Fig. 1 Schematic diagram of the solvated structure and the deposition process of Zn^{2+} in different electrolytes: (a) 2 M $ZnSO_4$ electrolyte, (b) mixed electrolyte containing HU.

stirrer and stir until fully dissolved. Weigh (or use a micropipette to measure) the required additives (0 M, 0.1 M, 0.2 M, 0.4 M HU) and add them to the glass bottle containing the initial electrolyte. Continue stirring on the magnetic stirrer until fully dissolved. Label the bottle for later use.

2.2 Preparation of electrodes

Firstly, mix the cathode active material (α-MnO_2), carbon black conductive agent, and polyvinylidene fluoride (PVDF) binder in a mass ratio of 7 : 2 : 1. Place the mixture in a mortar and grind it for approximately 30 minutes until it is fully uniform. Add an appropriate amount of *N*-methyl-2-pyrrolidone (NMP) and continue grinding for more than 30 minutes to form a uniform slurry. Use carbon cloth as the current collector, and apply the ground slurry evenly onto the carbon cloth using a scraper. Place it in a vacuum drying oven at 40 °C and dry it under vacuum for 6 hours. After removal, cut the dried carbon cloth into small circular discs with a diameter of 1.2 cm using a press machine. Before and after the coating process, weigh the carbon cloth and record its mass. Also, the area of the carbon cloth was measured, and the coating amount was calculated per unit area. Multiply 70% of the coating amount per unit area by the area of the small circular disc to determine the loading amount of the active material.

2.3 Negative electrode of aqueous zinc-ion battery

The negative electrode of the aqueous zinc-ion battery is a zinc sheet. Firstly, the purchased zinc sheet is polished sequentially with 3000, 5000, and 8000-grit sandpaper to remove surface oxides and other impurities. The sheet is then washed several times with distilled water and anhydrous ethanol. After thorough cleaning, the zinc sheet is placed in a drying oven to dry. Once dried, the zinc sheet is cut into small circular discs with a diameter of 1.2 cm using a press machine, and set aside for later use.

2.4 Assembly of aqueous zinc-ion battery

The battery assembled in this study is a 2032-type coin cell. The assembly sequence of the battery is as follows: negative electrode shell, spring clip, gasket, zinc sheet, separator (glass fiber/nonwoven fabric), electrolyte, positive electrode (zinc sheet or carbon cloth loaded with MnO_2), positive electrode shell. After assembly, the battery is sealed using a coin cell sealing machine at a pressure of 50 MPa. After sealing, wipe the battery surface, check the seal for integrity, and ensure that there is no leakage.

2.5 Characterization tests

Characterization of the zinc anode after cycling is performed using X-ray diffraction (XRD) to examine the deposition on different crystal planes and the formation of byproducts. Scanning electron microscopy (SEM) and energy-dispersive X-ray spectroscopy (EDS) are used to characterize the surface morphology and element distribution of the zinc anode after soaking and cycling. Fourier transform infrared (FTIR) spectroscopy, Raman spectroscopy, X-ray photoelectron spectroscopy (XPS), and nuclear magnetic resonance (NMR) are used to characterize the electrolyte at different concentrations and the soaked zinc foil. *In situ* optical microscopy and atomic force microscopy (AFM) are employed to characterize the dendrite growth and the surface roughness. Hydrogen production and rate are characterized using a high gas-tightness automatic online photocatalysis analysis system (Labsolar-6A).

2.6 Electrochemical tests

Constant current charge and discharge tests on Zn//Zn symmetric cells, Zn//MnO_2 full cells, and pouch cells using

the battery testing system (Land Testing System). Coulombic efficiency and nucleation potential tests on Zn//Cu asymmetric cells using the battery testing system (Neware BTS Testing System). Tafel, cyclic voltammetry (CV), linear sweep voltammetry (LSV), electrochemical impedance spectroscopy (EIS), and chronoamperometry (CA) tests using the electrochemical workstation.

2.7 Theoretical calculations

The theoretical calculations used in this study were all performed using Materials Studio.

The binding energy between the anode surface and solvent molecules, the electrostatic potential, the binding energy between Zn^{2+} and the solvent, as well as the LUMO and HOMO energy levels, were calculated using the DMol3 package in Materials Studio. The exchange and correlation terms were determined using the Generalized Gradient Approximation (GGA) and Perdew–Burke–Ernzerhof (PBE) functional. The energy convergence criterion was set to 10^6 hartree. This simulation studied the Zn (002) and Zn (100) crystal planes. A vacuum of approximately 15 Å along the *Z*-direction was added to eliminate the effects of periodic boundary conditions in the slab model. The 4×4 supercells of the Zn (002) and Zn (100) surfaces were used to represent the adsorption surfaces. The binding energy calculation formula is as follows:

$$E_{\text{adsorb/bind}} = E_{\text{A+B}} - E_{\text{A}} - E_{\text{B}} \quad (1)$$

where $E_{\text{adsorb/bind}}$ represents the adsorption/binding energy, $E_{\text{A+B}}$, E_{A} and E_{B} represent the total energy of the system and the energy of components A and B, respectively. A and B represent the interface, Zn^{2+}, additive molecules, anions, or H_2O molecules.

Molecular Dynamics (MD) simulations were performed using the Forcite module to study the solvation structure of Zn^{2+} in different electrolytes. The model was constructed with a specified number of H_2O, $ZnSO_4$, and additive molecules. The COMPASS II force field was used to assign charges to Zn^{2+}, H_2O, anions, and additives. Initially, geometry optimization was performed in the Forcite module based on a total energy convergence of 0.0001 kcal mol^{-1} and force convergence of 0.005 kcal mol^{-1} $Å^{-1}$. Afterward, MD simulations were conducted using the NVT and NPT ensembles at 298 K. The cutoff distance for van der Waals and electrostatic interactions was set to 15.5 Å. All simulations were performed under standard periodic boundary conditions, with a simulation time sufficiently long to ensure the electrolyte system reached an equilibrium state.

3 Results and discussions

The cost-effective hydroxyurea (HU) molecule is widely used in healthcare applications. Leveraging this, we applied HU innovatively as a functional additive in the battery field. The electrostatic potential (ESP) of HU (Fig. S3a†) shows that its electron density is primarily concentrated around the carbonyl oxygen atom. Compared to water molecules (Fig. S3b†), HU has stronger electronegativity, suggesting superior nucleophilic sites conducive to cation binding and hydrogen bonding.

3.1 Study of zinc ion solvation structure and hydrogen bond network

Fig. 2a illustrates the O–H bond bending (1500–1800 cm^{-1}) vibration in the Fourier-transform infrared (FTIR) where increasing HU content shifted this vibration to a higher wavenumber, while the stretching vibration shifted to a lower wavenumber (Fig. S4†), indicating a decrease in the bound water content. Further analysis is conducted using Raman spectroscopy and nuclear magnetic resonance (NMR) tests. The original Raman spectra (Fig. 2b) show O–H bond stretching vibrations (ν(O–H)) at different HU concentrations. As HU content increases, the peak between 3100 cm^{-1} and 3300 cm^{-1} shifted to lower wavenumbers, and the peak between 3300 cm^{-1} and 3500 cm^{-1} shifted to higher wavenumbers. More significantly, it also reveals three distinct peaks corresponding to strong (O–H1), medium (O–H2), and weak (O–H3) hydrogen bonds. Fitting the data shows changes in deconvoluted peak areas (Fig. S4†) and variations in hydrogen bond proportions (Fig. 2c). With increasing HU content, the proportion of strong hydrogen bonds rose from 46.9% to 51.5%, while medium and weak bonds decreased. These results not only demonstrate that HU can replace the coordinated water in the solvation structure of Zn^{2+} and release it into the bulk solution,[42–44] reducing water activity but also confirm that the carbonyl group (C=O) in HU can effectively disrupt the weak hydrogen bonds between water molecules and reconstruct a stronger hydrogen bond network with these water molecules. Additionally, the downfield shift in the hydrogen peak of the ^1H NMR spectrum (Fig. 2d) (especially when the concentration of HU reaches 0.2 M, the shift becomes more significant) confirms reduced bound water activity and the disruption of intrinsic hydrogen bonds by the carbonyl group.

Utilizing the Arrhenius equation ($1/R_{\text{ct}} = A\exp(-E_{\text{a}}RT)$) to analyze the EIS results (Fig. S6a and b†) the activation energy (E_{a}) for the 0.2 M HU-ZNS electrolyte was determined to be 23.15 kJ mol^{-1}, which is lower than the 29.64 kJ mol^{-1} observed in pure ZNS electrolyte (Fig. 2e). This finding indicates that the HU additive promotes Zn^{2+} desolvation and rapid ion transport from a thermokinetics perspective. Fig. S7† further supports this, showing that with HU concentrations of 0.1 M and 0.2 M, the amount of Zn^{2+} transport is significantly higher than in the control sample. This is due to the strong interactions between HU molecules and Zn^{2+}, which provide a fast transport pathway. However, at an HU concentration of 0.4 M, the increased viscosity of the solution reduces Zn^{2+} transport. Therefore, considering various factors, we chose 0.2 M as the optimal amount of the additive.

Subsequently, density functional theory (DFT) calculations and molecular dynamics simulations (MD) were performed to further elucidate HU's role in modulating the solvation structure of zinc ions. Firstly, we calculated the binding energies between Zn^{2+}, H_2O, and HU molecules using DFT. As shown in Fig. 2f, the binding energy between Zn^{2+} and HU ($|-158.33|$ eV)

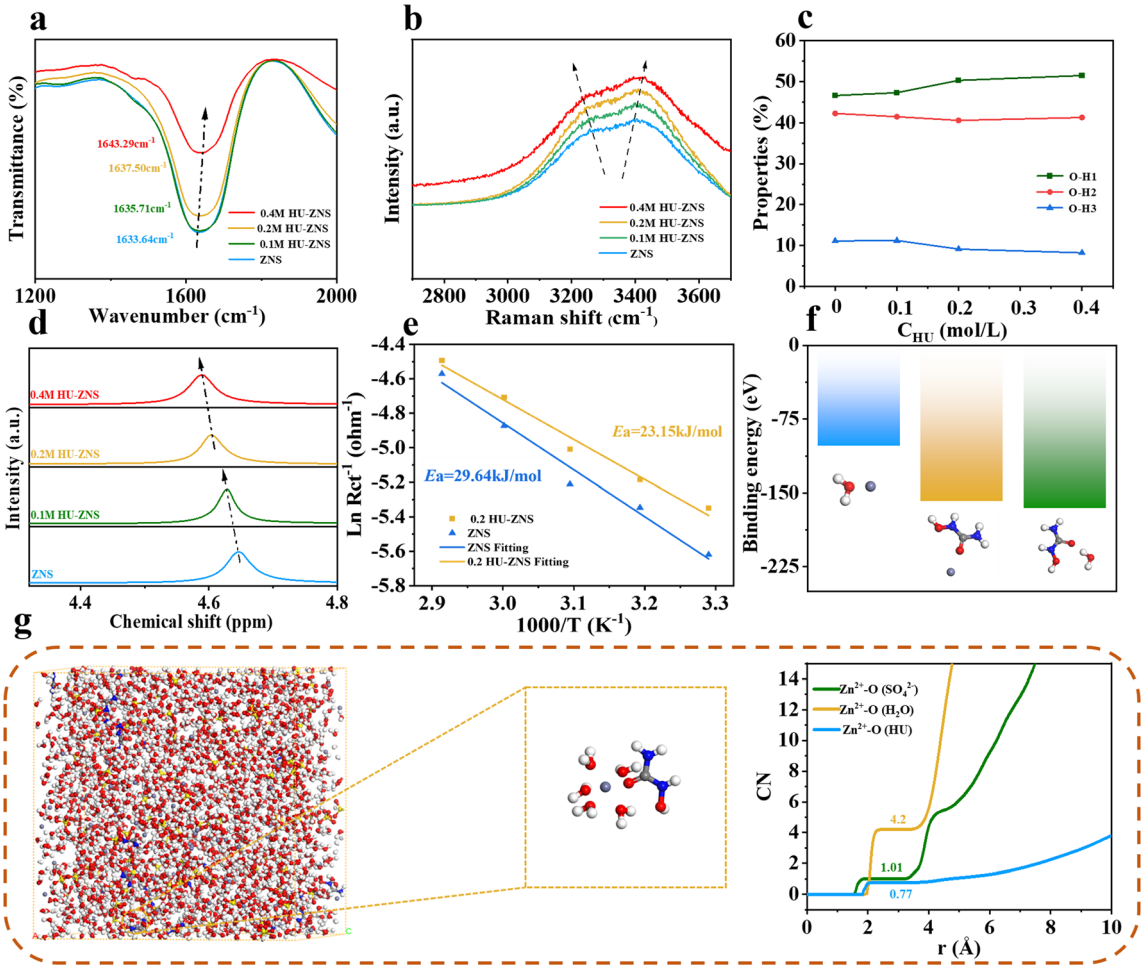

Fig. 2 (a) FTIR spectra of HU with different concentrations. (b) Raman spectrum of HU with different concentrations. (c) Hydrogen bond proportions are based on Raman fitting. (d) ^{1}H-NMR spectrum of HU with different concentrations. (e) E_a of hydrated Zn^{2+}. (f) Binding energy of Zn^{2+} with H_2O, and HU. (g) MD simulation image and CN diagram.

exceeds the solvation energy of Zn^{2+} (|−102.5| eV). This indicates that, under the influence of zinc-affinitive groups in HU, HU has a higher theoretical likelihood of integrating into the Zn^{2+} solvation sheath. Moreover, the binding energy between HU and H_2O (|−165.74| eV) significantly exceeds that between Zn^{2+} and H_2O, suggesting that HU molecules, influenced by the carbonyl group (C═O), are theoretically capable of disrupting the intrinsic hydrogen bond network and reconstructing a stronger one. Molecular dynamics (MD) simulations were further performed to investigate the solvation structure of Zn^{2+} in different systems with and without HU. As shown in Fig. S8,† in the pure ZNS electrolyte, the Zn^{2+} coordinates with six H_2O molecules in a typical manner. In contrast, when HU is added to the electrolyte, one of the coordinating H_2O molecules is replaced by an HU molecule, as shown in Fig. 2g. To better understand the solvation structure, the coordination number (CN) distribution function is analyzed. In the pure ZNS electrolyte, the average coordination number of H_2O molecules around Zn^{2+} in the solvation shell is approximately 5.3, as depicted in Fig. S9.† However, in the 0.2 M HU-ZNS mixed electrolyte, this coordination number decreases to 4.2 (Fig. 2g). These computational results suggest that the solvation structure of zinc ions transitions from $[Zn(H_2O)_6]^{2+}$ to $[Zn(H_2O)_5HU]^{2+}$.

3.2 Study of electric double-layer structure modification

To investigate the effect of HU molecules in the EDL, DFT simulations are conducted to examine the adsorption behavior of HU molecules on the Zn (002) crystal plane (Fig. 3a). Results indicate that regardless of adsorption at hollow, top, or bridge sites on the Zn (002) plane, the adsorption energy of HU was consistently lower than that of water. This demonstrates that HU molecules preferentially adsorb onto the anode surface over water molecules, providing a theoretical basis for the formation of a water-poor-content interface in the IHP of the EDL. HOMO and LUMO calculations (Fig. 3b) are also performed to study HU's charge transfer tendencies. The narrower band gap of HU (2.59 eV) compared to water's 7.53 eV indicates a higher propensity for electron loss, facilitating their reductive decomposition on the electrode more readily than the HER of free water. Additionally, compared to previously reported additives in the urea compound family (Fig. S10†), HU exhibits

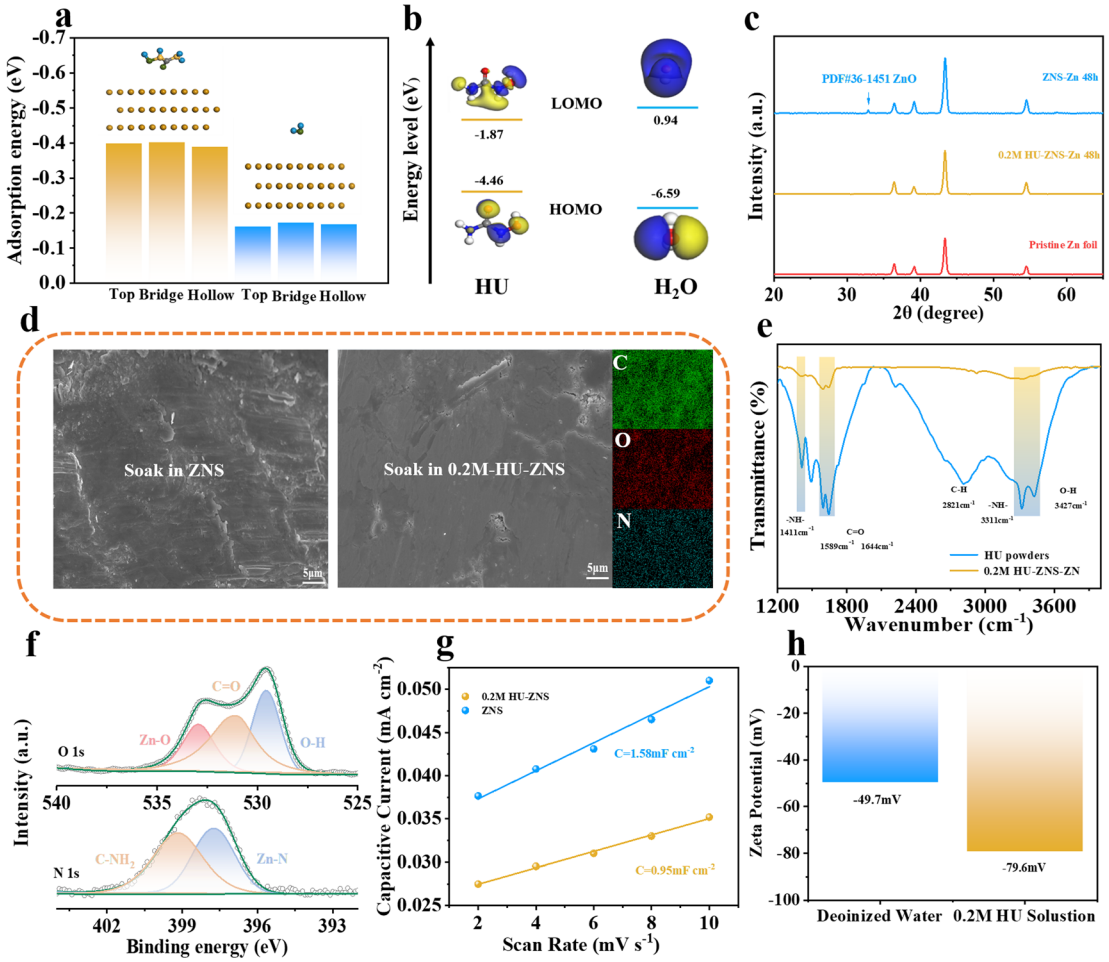

Fig. 3 (a) Adsorption modes and corresponding adsorption energies of H_2O and HU in different states on a Zn (002) plane. (b) HOMO and LOMO energy of HU and H_2O. Zn foils were immersed in different electrolytes for 48 hours: (c) XRD; (d) SEM and EDS; (e) ATR-FTIR. (f) XPS image of the zinc foil after being immersed in the HU-ZNS electrolyte for 48 hours. (g) EDLC curves of different electrolytes. (h) Zeta potential of deionized water and HU solution.

a narrower band gap and stronger adsorption onto the electrode surface.

To further clarify the adsorption capacity of HU, Zn foils are immersed in the ZNS solution and HU-ZNS solution for 48 hours. A grayish-white film is observed on the surface of HU-ZNS-Zn, in contrast, the zinc foil soaked in ZNS shows no changes (Fig. S11†). Fig. 3c presents the X-ray diffraction (XRD) patterns of the original Zn foil and those immersed in different electrolytes respectively. Compared to the original Zn foil, the XRD pattern of ZNS-Zn exhibits a distinct byproduct peak at approximately 32.88°. In contrast, the Zn foil immersed in the mixed electrolyte shows no significant byproducts. Furthermore, scanning electron microscopy (SEM) observations reveal that the surface of the zinc foil immersed in pure ZNS solution exhibits significant corrosion, becoming rough and uneven. In contrast, the zinc foil immersed in the mixed electrolyte showed a smoother and more uniform surface. Additionally, energy-dispersive spectroscopy (EDS) mapping indicates that C, N, and O elements are evenly distributed across the Zn anode surface following immersion in the mixed electrolyte (Fig. 3d). The attenuated total reflectance Fourier-transform infrared (ATR-FTIR) spectra of Zn foil immersed in the mixed electrolyte and pure HU powder (Fig. 3e) exhibits similar peaks. The C=O stretching vibration peaks at 1589 cm^{-1} and 1644 cm^{-1} in HU powder shifted to higher wavenumbers in the Zn foil post-immersion. The peaks at 3311 cm^{-1} and 3427 cm^{-1} correspond to –NH– stretching vibrations (in amino ($–NH_2$) or amide (–NH–CO) groups) and O–H stretching vibrations. Interestingly, the intensities of both decrease after coordination. This indicates that HU molecules coordinate with the Zn metal surface and are anchored to it stably. Raman spectroscopy and XPS further support the above analysis. As shown in Fig. S12,† the characteristic peaks associated with the –NH– groups in HU are still observed in the Raman spectrum of HU-ZNS-Zn. XPS analysis is conducted on the surface of zinc foil immersed in HU-ZNS. The presence of C–NH_2 and Zn–N peaks in the N 1s spectrum, along with O–H, C=O, and Zn–O peaks in the O 1s spectrum (Fig. 3f), provides compelling evidence for the strong adsorption of HU on the zinc foil surface. Furthermore, compared to zinc foil soaked in the ZNS electrolyte, the Zn 2p binding energy of the zinc foil in the mixed electrolyte shifted by 1.5 eV towards higher energy (Fig. S13†). These findings confirm

that HU preferentially adsorbs onto the Zn anode surface, forming a water-poor IHP.

To confirm the electrochemical perspective of the EDL structure adjustment by HU, we assembled a Zn–Zn symmetrical cell using both pure ZNS and mixed electrolytes and performed CV tests at various scan rates (Fig. S14a and b†). The results are fitted according to the equation $C = i/v$, resulting in electric double-layer capacitance (EDLC) curves utilized to examine changes in EDL capacitance related to charged characteristics. Fig. 3g illustrates that the capacitance of the cell utilizing the mixed electrolyte (0.95 mF cm^{-2}) is significantly lower than that of the cell using the ZNS electrolyte (1.58 mF cm^{-2}). It is known that highly polar water molecules tend to form a directional dipole layer within the intrinsic EDL, which is difficult to break, due to strong interactions among water molecules. This layer is called the compact hydration layer (IHP), whereas the OHP represents a residual charge layer. Experimental results indicate that polar HU molecules, due to their highly electron-dense functional groups, disrupt intrinsic hydrogen bonds within the IHP, partially replacing the dense hydration layer in the double layer. It is important to note that capacitance is generally inversely proportional to the effective thickness of the EDL. Therefore, when the relatively large HU molecules replace some of the H_2O molecules, the increased thickness of the EDL is expected to result in an obvious decrease in capacitance. According to EDL theory:[21]

$$\frac{1}{C_{CL}} = \frac{1}{C_{IHP}} + \frac{1}{C_{OHP}} \quad (2)$$

$$\frac{1}{C_{EDL}} = \frac{1}{C_{CL}} + \frac{1}{C_{DL}} \quad (3)$$

where C_{CL} is the capacitance of the compact layer, C_{IHP} is the capacitance of the IHP, C_{OHP} is the capacitance of the OHP containing hydrated cations/anions, C_{EDL} is the capacitance of the EDL, and C_{DL} is the capacitance of the diffusion layer. The diffusion layer is composed exclusively of residual charges produced during electrolyte diffusion and does not involve short-range forces, resulting in a uniform thickness.[21] The observed differences in capacitance curves can primarily be attributed to variations in the thickness of the compact layer. Similarly, as shown in Fig. S15† the differential capacitance (DC) decreases with the addition of the HU additive, indicating its involvement in the adjustment of the EDL structure. To further investigate the impact of the high electron-dense functional groups in HU on the EDL, we measured the ζ potential by dispersing nanoscale zinc powder in deionized water and 0.2 M HU aqueous solution *via* ultrasonication. As shown in Fig. 3h, the addition of HU led to a significant decrease in ζ potential, indicating the formation of a localized high electron density on the particle surface due to adsorption. This is because HU forms an adsorption layer on the zinc surface, and after partial dissociation (with primary dissociation occurring in the amide group), its high-electron-density functional groups, including the carbonyl and hydroxyl groups, enter the EDL, thereby reducing the particle potential.

3.3 Characterization of zinc anode corrosion and deposition performance

Building on the above analysis of HU's multi-functional effects, additional experiments were conducted to further validate its role in enhancing corrosion resistance and suppressing the HER. Tafel tests were conducted on Zn foil in both ZNS and mixed electrolytes. As shown in Fig. 4a, the addition of HU caused minimal changes in corrosion potential; however, the i_{corr} decreased markedly from 2.797 mA cm^{-2} to 0.490 mA cm^{-2}, indicating HU's significant inhibitory effect on corrosion. HER suppression was further investigated using LSV. As shown in Fig. 4b, the HER potential shifted from −0.131 V to −0.157 V with the addition of HU, reflecting a higher threshold for HER initiation induced by active water, further confirming HU's strong inhibitory effect on HER. To visually assess the HER, a transparent Zn//Zn symmetric cell (inset of Fig. 4b) was assembled at a current density of 2 mA cm^{-2}, 1 mA h cm^{-2}. After 50 cycles, the Zn anode in the pure ZNS electrolyte exhibited significant bubble formation due to HER, whereas no noticeable H_2 generation was observed in the cell with the mixed electrolyte. Furthermore, as shown in Fig. S16,† *in situ* hydrogen evolution tests reveal that the hydrogen production rate significantly decreases after the addition of HU. These align with the results discussed in the LSV.

The beneficial impact of HU on diffusion patterns and Zn deposition was further confirmed through CV and CA measurements. Classical nucleation theory suggests higher nucleation overpotential (NOP) leads to smaller grain sizes during Zn deposition.[45] As shown in Fig. 4c, the NOP of the mixed electrolyte is 35 mV higher than that of pure ZNS, indicating that HU molecules promote finer and more uniform nucleation of zinc, thereby enhancing deposition kinetics. This effect may result from HU molecules displacing some active water molecules and occupying the IHP, acting as an electrostatic shielding layer, thus increasing the Zn^{2+} deposition barrier needed to initiate Zn nucleation. Additionally, with the addition of HU, the redox peak intensities in the CV curve decrease, suggesting that the intrinsic coordination reaction of Zn^{2+} within the electrolyte is hindered. This decrease in reaction kinetics further corroborates HU's role in modifying the solvation structure of Zn^{2+}. Fig. S17† presents the CA curves of Zn//Zn symmetric cells assembled with pure ZNS and mixed electrolytes under a constant cathodic potential of −150 mV. In the first 400 seconds, the current in both cells increases rapidly, indicating a rapid 2D diffusion nucleation process. The absorbed Zn^{2+} preferentially diffuses laterally along the surface, clustering into dendritic formations to minimize surface energy and exposed area.[46] After 400 seconds, in the electrolyte containing the HU additive, the current growth rate decreases significantly, indicating a transition toward 3D diffusion. This transition was attributed to enhanced deposition kinetics of Zn ions and their preferential deposition on the (002) crystal plane. In contrast, the cell with pure ZNS electrolyte continues in the 2D diffusion mode for over 1200 seconds, facilitating uncontrolled Zn dendrite growth and increasing the likelihood of side reactions.

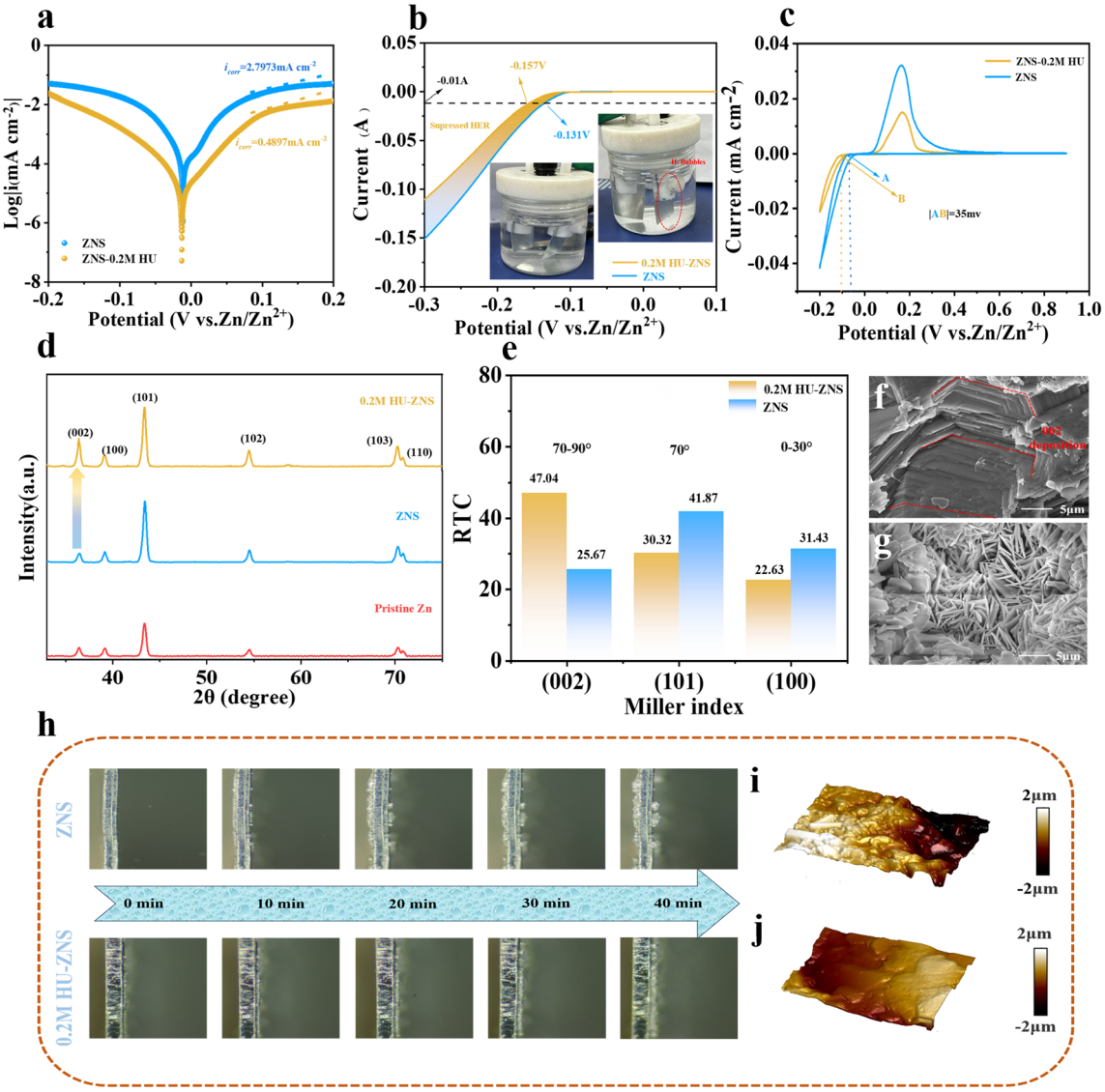

Fig. 4 (a) The Tafel plots in different electrolytes at a scan rate of 1 mV s^{-1}. (b) LSV curves in different electrolytes. (c) CV curves in different electrolytes at a scan rate of 1 mV s^{-1}. (d) XRD patterns of Zn anode after cycling in different electrolytes. (e) The RTC of Zn anodes cycling in different electrolytes. (f) ZNS electrolyte. SEM images of the Zn foil surface after cycling. (g) HU-ZNS electrolyte. SEM images of the Zn foil surface after cycling. (h) *In situ* optical microscopy observations of the Zn deposition process in ZNS electrolyte and HU-ZNS electrolyte. AFM images after cycling: (i) ZNS electrolyte; (j) HU-ZNS electrolyte.

To investigate the role of HU molecules in promoting Zn^{2+} deposition on the (002) crystal plane during cycling, X-ray diffraction (XRD) analysis was performed to examine the deposition behavior on the anode surface after 48 cycles at a current density of 5 mA cm^{-2} in symmetric cells with different electrolytes. As shown in Fig. 4d, the Zn anode in the ZNS sample displayed reduced (002) crystal plane intensity relative to the (100) plane compared to pristine zinc foil. Conversely, the Zn anode with the HU-containing electrolyte exhibited a markedly increased (002) crystal plane intensity, surpassing that of the (100) plane. This observation indicates that in the ZNS sample, the (100) and (101) planes preferentially grew, whereas the (002) plane growth was inhibited. In contrast, adding HU molecules induced preferential growth of the (002) plane on the Zn anode. To quantify these observations, the relative texture coefficients (RTC) were calculated using the formula:[47]

$$\mathrm{RTC}_{(hkl)} = ((I_{(hkl)}/I_{0(hkl)})/\sum(I_{(hkl)}/I_{0(hkl)})) \times 100 \quad (4)$$

A higher RTC value represents a more dominant texture on the corresponding crystal plane,[48,49] as shown in Fig. 4e, the addition of 0.2 M HU increased the RTC of the (002) plane from 25.67 to 47.04, while the RTC of the (100) and (101) planes decreased from 31.43 to 22.63 and 41.87 to 30.32, respectively. Similarly, as shown in Fig. S18,† under the same concentration of HU additive, the intensity of the (002) crystal plane increases with the number of cycles, after 100 cycles, the intensity of the (002) crystal plane is even three times that of the (100) crystal

plane. We used SEM to observe the surface of the anode after cycling, further confirming the inductive effect of HU on Zn^{2+} at the (002) crystal plane. In the pure ZNS electrolyte, due to the "tip effect" and uneven deposition, the anode surface became densely covered with needle-like Zn dendrites (Fig. 4g). This not only increases the risk of separator piercing and subsequent short circuits but also substantially reduces the anode's reversibility. In contrast, with the addition of HU, Zn^{2+} on the Zn anode surface exhibits uniform homoepitaxial deposition in a hexagonal layered structure (Fig. 4f), consistent with the (002) crystal plane deposition behavior. To investigate this mechanism, we calculated the adsorption energy of HU on different crystal planes. As shown in Fig. S19,† HU exhibits higher adsorption energy on the (002) crystal plane compared to the (100) plane. This suggests that HU preferentially adsorbs on the (002) plane, where the dissociated carbonyl and amine groups, with their high electron density, attract Zn^{2+}, promoting their uniform deposition on the (002) plane.

In situ optical microscopy was also employed to continuously observe the morphological evolution of the anode during the plating/stripping cycles, providing real-time insights into the zinc deposition process. As illustrated in Fig. 4h, the pure ZNS/Zn anode exhibited the formation of small protruding zinc dendrites after just 10 minutes of plating. These dendrites, initially appearing as irregular and spiky protrusions, continued to grow and elongate with ongoing plating, while bubble formation was also observed on the anode surface during the process. After 40 minutes of plating, the dendrites had developed into large, branched structures that accumulated on the deposition layer, resulting in an increasingly rough and uneven surface. This dendritic growth was accompanied by a significant increase in surface roughness, which is detrimental to the overall performance and longevity of the anode. In contrast, the introduction of the HU additive into the electrolyte had a remarkable effect on the zinc deposition behavior. Throughout the entire 40 minute plating period, the zinc anode in the HU-modified electrolyte maintained a smooth, uniform deposition layer with no visible dendrite formation or bubble generation. The absence of irregular protrusions or surface instabilities indicates that HU effectively regulates the plating process, promoting a more controlled and stable deposition of zinc ions onto the anode, mitigating side reactions.

To further evaluate the effect of the HU additive on the surface morphology of the zinc anode, atomic force microscopy (AFM) was utilized to assess the roughness of the anode in different electrolytes quantitatively. As shown in Fig. 4i and j, the anode in the pure ZNS electrolyte exhibited significant surface height fluctuations, with clear dendritic features and pronounced roughness. This was in stark contrast to the anode in the HU-containing electrolyte, which displayed a much smoother and more uniform surface profile. The AFM results confirmed that the roughness of the Zn anode in the HU-modified electrolyte was significantly lower, suggesting that HU not only prevents dendrite formation but also reduces the occurrence of parasitic side reactions, thereby ensuring a more uniform and stable surface morphology.

3.4 Study of zinc anode reversibility and stability

To assess the effect of the HU additive on anode reversibility, Zn//Cu asymmetric batteries were assembled at a current density of 1 mA cm^{-2} with a capacity of 0.5 mA h cm^{-2}. As shown in Fig. 5a, the asymmetric cells utilizing pure ZNS electrolyte failed after less than 200 cycles. Moreover, the corresponding voltage profile (Fig. 5b) exhibited significant instability, with fluctuations observed throughout the cycling process. This instability can be attributed to the uncontrolled growth of Zn dendrites and instability at the solid–liquid interface during long cycling, leading to excessive HER and subsequent short circuits. However, the incorporation of 0.2 M HU significantly enhanced battery performance, enabling stable cycling for over 1600 cycles with an average coulombic efficiency of 99.34%. The corresponding voltage profile also exhibited high stability. It should be noted that although the CE of both systems is slightly above 100% in the early cycles, this is mainly due to the formation of metastable or unstable zinc compounds, which release additional electrons during discharge. Additionally, under identical charging and discharging conditions (1 mA cm^{-2}, 0.5 mA h cm^{-2}), the nucleation overpotential on copper foil with added HU (103 mV) is significantly higher than that without HU (51 mV) (Fig. S20†). This increase suggests that HU promotes finer and more uniform zinc nucleation on the current collector, contributing to the long-term cycling stability of the Zn//Cu cell.

Zn//Zn symmetric cells were assembled to evaluate the long-term cycling stability of the Zn anode. As shown in Fig. 5d, the Zn//Zn symmetric cell with the mixed electrolyte demonstrates stable Zn plating/stripping performance across various rates. In contrast, the cell with pure ZNS electrolyte experiences short-circuit failure at 5 mA cm^{-2}. Fig. 5c displays the long-term cycling performance of Zn//Zn symmetric cells under a low current density (1 mA cm^{-2}, 0.5 mA h cm^{-2}) with different electrolytes. The cell with the mixed electrolyte achieved stable cycling for up to 2600 hours. Conversely, the cell with ZNS electrolyte experienced multiple short-circuit failures within 500 hours, rendering it unsuitable for prolonged cycling. Similarly, under a current density of 3 mA cm^{-2} (Fig. S21†), a similar phenomenon was observed. The symmetric cell composed of pure ZNS experienced a short circuit in less than 100 hours, while the symmetric cell with the addition of HU maintained stable cycling for over 1000 hours.

To further evaluate the performance of Zn//Zn symmetric cells with the mixed electrolyte under challenging conditions, tests were conducted at a high current density (10 mA cm^{-2}) and extremely low temperatures. As shown in Fig. 5e, the mixed electrolyte cell exhibited highly reversible and stable Zn plating/stripping for up to 265 hours under high current density. At −25 °C (Fig. 5f), the cell using pure ZNS electrolyte experienced uncontrolled polarization voltage after approximately 100 hours, leading to the failure. This failure is attributed to the ordered freezing structure formed by abundant hydrogen bonds among water molecules, resulting in solidification of the ZNS electrolyte and severe hindrance to Zn^{2+} migration. However, as previously mentioned, the addition of HU disrupts the weak

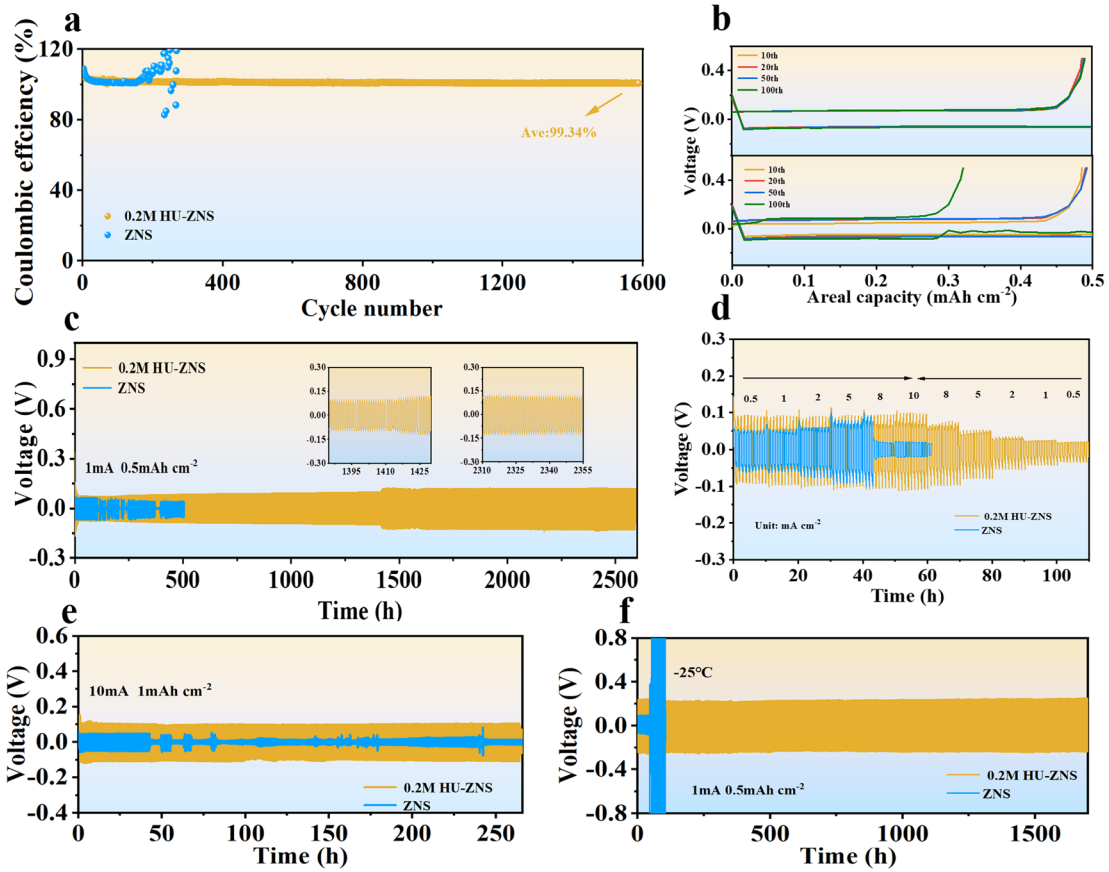

Fig. 5 (a) CE of Zn//Cu asymmetric cell. (b) The voltage–capacity curves for the selected cycles in different electrolytes. (c) Cycling stability of Zn//Zn symmetric cell at 1 mA cm^{-2}. (d) Rate performance of Zn//Zn symmetric cells. (e) Cycling stability of Zn//Zn symmetric cell at 10 mA cm^{-2}. (f) Cycling stability of Zn//Zn symmetric cell at 1 mA cm^{-2} under −25 °C.

hydrogen bonds between water molecules and reconstructs a stronger hydrogen bond network. This adjustment lowers the freezing point and enhances ion mobility, enabling the mixed electrolyte cell to achieve stable cycling for over 1700 hours at −25 °C. Interestingly, under all conditions tested, the symmetric cells with HU-containing electrolytes exhibited higher polarization voltage than those with pure ZNS electrolytes, reflecting enhanced Zn^{2+} deposition kinetics.

3.5 Study of Zn//MnO_2 full cell performance

Finally, the full cell was assembled with carbon paper loaded with α-MnO_2 as the cathode material to evaluate the electrochemical performance of Zn anodes in different electrolytes (Fig. 6a). As shown in Fig. 6b, the MnO_2 full cell with HU containing electrolyte demonstrated excellent rate performance`, achieving a specific capacity of 226.3 mA h g^{-1} at 0.5 A g^{-1} and maintaining 124 mA h g^{-1} at 5 A g^{-1}. It also showed high coulombic efficiency throughout the test. In contrast, the full cell with pure ZNS electrolyte exhibited rapid capacity decay across different current densities, retaining only 38 mA h g^{-1} at higher current densities. This can be attributed to the insufficient suppression of parasitic reactions and byproducts. At high current density, OH^- generated by HER leads to localized alkalization of the electrolyte, causing byproducts to deposit on the electrode surface, forming a passivation layer that hinders ion transport, slows reaction kinetics and reduces rate performance. Moreover, the accumulation of parasitic reactions significantly depletes active materials and electrolytes, reducing capacity retention at high current density. The corresponding galvanostatic charge/discharge (GCD) curves in Fig. 6c show a pair of distinct platforms with minimal variations, indicating rapid reaction kinetics and effective suppression of side reactions. The self-discharge behavior of the battery in a fully charged state can effectively reflect the parasitic reactions in the full cell.[50] As shown in Fig. 6e, the capacity retention of Zn//MnO_2 full cells with different electrolytes was tested after being fully charged and left to stand for 24 hours. After the same resting period, the full cell with pure ZNS electrolyte showed a capacity retention of only 86.5%, while the full cell with HU-added electrolyte exhibited a significantly improved capacity retention of 95.4%. The HER and various parasitic reactions induced by hydrated water on the anode surface likely caused zinc corrosion, which exacerbated the self-discharge of AZIBs.[51] The addition of HU effectively suppressed these reactions by modulating hydrogen bonds and the EDL structure, thereby reducing the self-discharge of the full cell. In long-cycle tests, the full cell with the mixed electrolyte maintained a capacity retention of 86.88% over 1400 cycles, with a remarkable coulombic efficiency stabilized at 99.8%. In

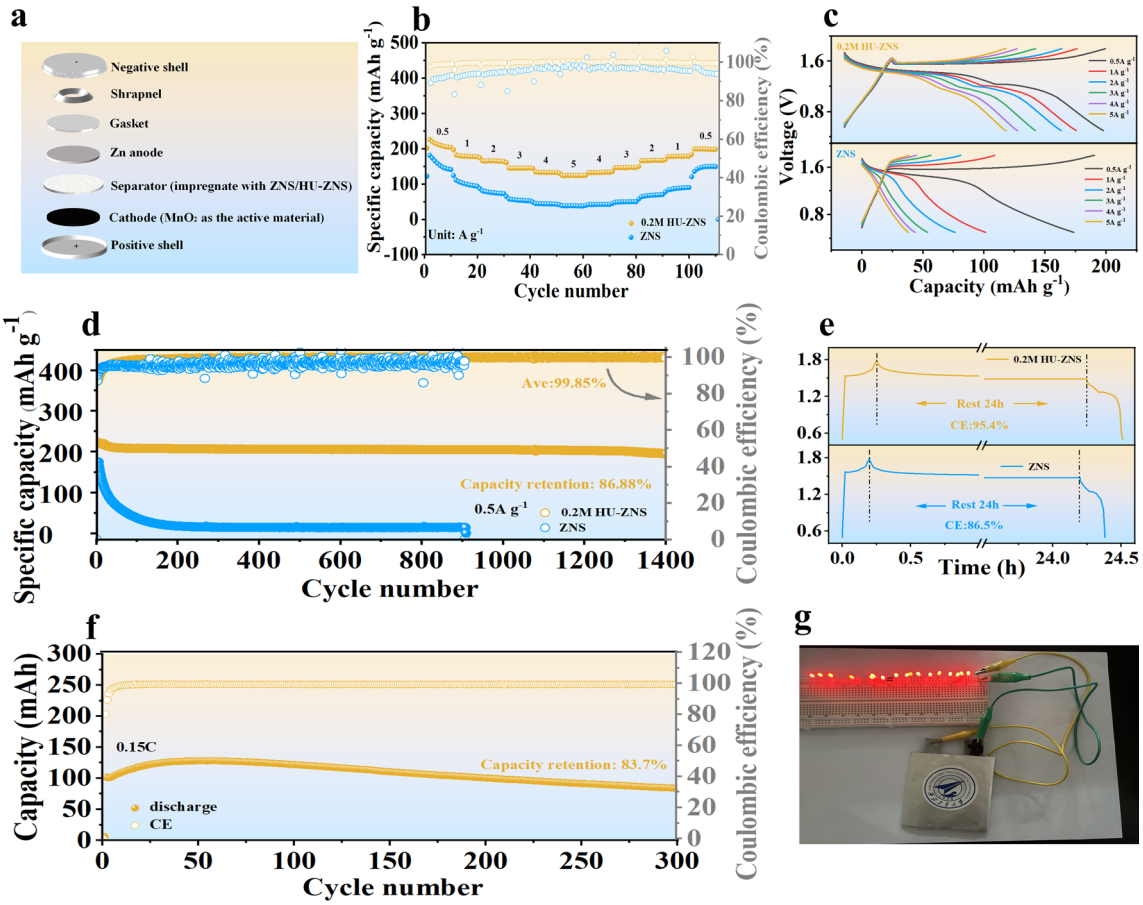

Fig. 6 (a) Schematic illustration of the full cell configuration. (b) Rate performance. (c) The GCD curves. (d) Cycling stability of Zn//MnO_2 coin cell at 0.5 A g^{-1}. (e) Self-discharge curves at 1 A g^{-1}. (f) Cycling stability of assembled 5 × 6 cm^2 Zn//MnO_2 pouch battery. (g) The application of as a power source for small lights.

contrast, the full cell with pure ZNS electrolyte showed a rapid decline in capacity retention within only a few hundred cycles (Fig. 6d). Additionally, at a high current density of 3 A g^{-1}, the Zn//MnO_2 full cell with HU addition also maintained a capacity retention of 86.71% after 2000 cycles (Fig. S22†). Subsequently, we conducted SEM to observe the surface morphology of the anode. As shown in Fig. S23,† the anode cycled with pure ZNS electrolyte showed severe corrosion and a moss-like rough surface due to parasitic reactions. In contrast, the anode with HU-added electrolyte exhibited a smooth, uniform surface.

To assess the commercial potential of the battery after the addition of HU, we assembled a Zn//MnO_2 soft-pack battery with dimensions of 5 cm × 6 cm and an N/P ratio of 7.6. As shown in Fig. 6f, the initial capacity of the Zn//MnO_2 soft-pack battery was 104.7 mA h, and after 300 cycles at a current density of 0.15 C, it retained 83.7% of its initial capacity with stable coulombic efficiency. Additionally, as shown in Fig. S24† the battery exhibited a high open-circuit voltage of 1.69 V and successfully powered 17 small light bulbs when connected to a circuit (Fig. 6g and S25†). These results demonstrate the potential of Zn//MnO_2 pouch batteries as a safe and reliable energy storage device.

4 Conclusions

In summary, hydroxyurea (HU) was introduced as an additive to optimize both the electric double layer (EDL) and solvation structure of Zn^{2+} in aqueous zinc-ion batteries (AZIBs). HU's strong coordination with Zn^{2+} reshapes the solvation structure and forms a water-poor inner Helmholtz plane (IHP), effectively suppressing hydrogen evolution reactions (HER) and promoting uniform zinc ion deposition on the (002) crystal plane, thereby inhibiting the growth of zinc dendrites. Additionally, HU promotes the desolvation process of Zn^{2+}, facilitating faster reaction kinetics and uniform zinc deposition. The Zn//Zn symmetric cells with HU-modified electrolyte exhibit outstanding cycling stability, operating for over 2600 hours at 1 mA cm^{-2}, it still demonstrates impressive cyclic performance under harsh conditions. The Zn//MnO_2 full cells retain 86.88% of their initial capacity after 1400 cycles, and demonstrate an ultra-high coulombic efficiency of 99.8%, while the Zn//MnO_2 pouch cells show 83.7% capacity retention after 300 cycles. This study highlights HU as a promising, low-cost additive that enhances the performance and scalability of AZIBs, providing valuable insights into improving the stability and efficiency of zinc anodes in aqueous metal batteries.

Data availability

The datasets used and/or analyzed during the current study are available from the corresponding author upon reasonable request.

Author contributions

In this study, Rui-Zhe Zhang was responsible for the overall experimental design, material preparation, characterization, and electrochemical testing. Zhi-Yong Liao handled the simulation calculations. Hui-Qing Fan, Li-Xin Song, Qing-Feng Zhang, and Yong-Bo Fan provided guidance and revisions for the manuscript. Pei-Zhi Dong assisted with the *in situ* hydrogen generation tests. The other authors made various contributions to the research.

Conflicts of interest

There are no conflicts of interest in this study. All authors have read and approved this version of the article, and due care has been taken to ensure the integrity of the work. Neither the entire paper nor any part of its content has been published or accepted elsewhere. It is not being submitted to any other journal.

Acknowledgements

This work was supported by the National Nature Science Foundation (52372125, 52333009, 52272124), the Shanxi Provincial Science Foundation (2021GXLH-01-11), the Yulin Project (2022-19-11), the High-Quality Patent Cultivation Project (XGD2021-04), the Fundamental Research Funds for the Central Universities (D5000230071), and the 111 Program of MOE of China (B08040). We would also like to thank the Analytical & Testing Center of Northwestern Polytechnical University (2024T008). The author Y. Fan would like to thank the Open Project of Hubei Key Laboratory of Micro-Nanoelectronic Materials and Devices (No. KEY202407).

References

1 J. Yang, Y. Zhang, Z. Li, X. Xu, X. Su, J. Lai, Y. Liu, K. Ding, L. Chen, Y.-P. Cai and Q. Zheng, *Adv. Funct. Mater.*, 2022, **32**, 2209642.
2 A. Li, J. Li, Y. He and M. Wu, *J. Energy Chem.*, 2023, **83**, 209–228.
3 M. Shi, B. Wang, C. Chen, J. Lang, C. Yan and X. Yan, *J. Mater. Chem. A*, 2020, **8**, 24635–24644.
4 H. Wu, H. Yin, H. Tian, J. Yang and R. Liu, *Energy Environ. Mater.*, 2024, e12839.
5 J. Luo, L. Xu, Y. Yang, S. Huang, Y. Zhou, Y. Shao, T. Wang, J. Tian, S. Guo, J. Zhao, X. Zhao, T. Cheng, Y. Shao and J. Zhang, *Nat. Commun.*, 2024, **15**, 6471.
6 Q. Wen, H. Fu, R.-d. Cui, H.-Z. Chen, R.-H. Ji, L.-B. Tang, C. Yan, J. Mao, K.-H. Dai, X.-H. Zhang and J.-C. Zheng, *J. Energy Chem.*, 2023, **83**, 287–303.
7 Q. Zhang, Y. Ma, Y. Lu, Y. Ni, L. Lin, Z. Hao, Z. Yan, Q. Zhao and J. Chen, *J. Am. Chem. Soc.*, 2022, **144**, 18435–18443.
8 Y. Meng, M. Wang, J. Wang, X. Huang, X. Zhou, M. Sajid, Z. Xie, R. Luo, Z. Zhu, Z. Zhang, N. A. Khan, Y. Wang, Z. Li and W. Chen, *Nat. Commun.*, 2024, **15**, 8431.
9 H. Tian, J.-L. Yang, Y. Deng, W. Tang, R. Liu, C. Xu, P. Han and H. J. Fan, *Adv. Energy Mater.*, 2023, **13**, 2202603.
10 N. Hu, W. Lv, W. Chen, H. Tang, X. Zhang, H. Qin, D. Huang, J. Zhu, Z. Chen, J. Xu and H. He, *Adv. Funct. Mater.*, 2024, **34**, 2311773.
11 Y. Chai, X. Xie, Z. He, G. Guo, P. Wang, Z. Xing, B. Lu, S. Liang, Y. Tang and J. Zhou, *Chem. Sci.*, 2022, **13**, 11656–11665.
12 S.-B. Wang, Q. Ran, R.-Q. Yao, H. Shi, Z. Wen, M. Zhao, X.-Y. Lang and Q. Jiang, *Nat. Commun.*, 2020, **11**, 1634.
13 X. Xie, S. Liang, J. Gao, S. Guo, J. Guo, C. Wang, G. Xu, X. Wu, G. Chen and J. Zhou, *Energy Environ. Sci.*, 2020, **13**, 503–510.
14 X. Li, P. Ye, A. Dou, Z. Jiang, A. Naveed, Y. Zhou, M. Su, P. Zhang and Y. Liu, *J. Energy Storage*, 2024, **76**, 109874.
15 H. Li, C. Xu, C. Han, Y. Chen, C. Wei, B. Li and F. Kang, *J. Electrochem. Soc.*, 2015, **162**, A1439–A1444.
16 Y. Zeng, Z. Pei, Y. Guo, D. Luan, X. Gu and X. W. Lou, *Angew. Chem., Int. Ed.*, 2023, **62**, e202312145.
17 C.-X. Zhao, J.-N. Liu, B.-Q. Li, D. Ren, X. Chen, J. Yu and Q. Zhang, *Adv. Funct. Mater.*, 2020, **30**, 2003619.
18 H. Yin, H. Wu, Y. Yang, S. Yao, P. Han, Y. Shi and R. Liu, *Small*, 2024, **20**, 2404367.
19 Y. Lyu, J. A. Yuwono, P. Wang, Y. Wang, F. Yang, S. Liu, S. Zhang, B. Wang, K. Davey, J. Mao and Z. Guo, *Angew. Chem., Int. Ed.*, 2023, **62**, e202303011.
20 L. Jiang, L. Yao, G. Wang, C. Liu, X. Chi and Y. Liu, *J. Energy Chem.*, 2024, **60**, 778–785.
21 S. Cai, X. Chu, C. Liu, H. Lai, H. Chen, Y. Jiang, F. Guo, Z. Xu, C. Wang and C. Gao, *Adv. Mater.*, 2021, **33**, 2007470.
22 X. Wang, Z. Zhang, B. Xi, W. Chen, Y. Jia, J. Feng and S. Xiong, *ACS Nano*, 2021, **15**, 9244–9272.
23 P. Ruan, S. Liang, B. Lu, H. J. Fan and J. Zhou, *Angew. Chem., Int. Ed.*, 2022, **61**, e202200598.
24 Y. Dai, C. Zhang, W. Zhang, L. Cui, C. Ye, X. Hong, J. Li, R. Chen, W. Zong, X. Gao, J. Zhu, P. Jiang, Q. An, D. J. L. Brett, I. P. Parkin, G. He and L. Mai, *Angew. Chem., Int. Ed.*, 2023, **62**, e202301192.
25 R. Han, T. Jiang, Z. Wang, R. Xue, X. Liu, Y. Tang, Z. Qi and Y. Ma, *Adv. Funct. Mater.*, 2024, 2412255.
26 L. Jiang, D. Li, X. Xie, D. Ji, L. Li, L. Li, Z. He, B. Lu, S. Liang and J. Zhou, *Energy Storage Mater.*, 2023, **62**, 102932.
27 Y. Chen, Z. Deng, Y. Sun, Y. Li, H. Zhang, G. Li, H. Zeng and X. Wang, *Nano-Micro Lett.*, 2024, **16**, 96.
28 Y. Yang, H. Hua, Z. Lv, M. Zhang, C. Liu, Z. Wen, H. Xie, W. He, J. Zhao and C. C. Li, *Adv. Funct. Mater.*, 2023, **33**, 2212446.
29 K. Qi, P. Liang, S. Wei, H. Ao, X. Ding, S. Chen, Z. Fan, C. Wang, L. Song, X. Wu, C. Wu and Y. Zhu, *Energy Environ. Sci.*, 2024, **17**, 2566–2575.
30 Y. Lei, X. Liang, L. Yang, P. Jiang, Z. Lei, S. Wu and J. Feng, *J. Mater. Chem. A*, 2020, **8**, 4376–4385.

31 Y. Yang, H. Hua, Z. Lv, M. Zhang, C. Y. Liu, Z. Wen, H. Xie, W. He, J. Zhao and C. C. Li, *Adv. Funct. Mater.*, 2022, **33**, 2212446.
32 Z. Li, Y. Liao, Y. Wang, J. Cong, H. Ji, Z. Huang and Y. Huang, *Energy Storage Mater.*, 2023, **56**, 174–182.
33 P. Sun, L. Ma, W. Zhou, M. Qiu, Z. Wang, D. Chao and W. Mai, *Angew. Chem., Int. Ed.*, 2021, **60**, 18247–18255.
34 P. J. Chimtali, X. Yang, Q. Zhou, S. Wei, Z. Mohamed, H. Akhtar, A. Al-Mahgari, Y. Zhou, H. Xu, Z. Zhang, D. Cao, S. Chen, K. Zhu, X. Guo, H. Shou, X. Wu, C. Wang and L. Song, *Small*, 2024, **20**, 2400673.
35 T. C. Li, Y. Lim, X. L. Li, S. Luo, C. Lin, D. Fang, S. Xia, Y. Wang and H. Y. Yang, *Adv. Energy Mater.*, 2022, **12**, 2103231.
36 Q. Yang, L. Li, T. Hussain, D. Wang, L. Hui, Y. Guo, G. Liang, X. Li, Z. Chen, Z. Huang, Y. Li, Y. Xue, Z. Zuo, J. Qiu, Y. Li and C. Zhi, *Angew. Chem., Int. Ed.*, 2022, **61**, e202112304.
37 M. Han, T. C. Li, X. Chen and H. Y. Yang, *Small*, 2024, **20**, 2304901.
38 M. Wang, Y. Meng, P. Gao, K. Li, Z. Liu, Z. Zhu, M. Ali, T. Ahmad, N. Chen, Y. Yuan, Y. Xu, M. Chuai, J. Sun, X. Zheng, X. Li, J. Yang and W. Chen, *Adv. Mater.*, 2023, **35**, 2305368.
39 X. Zhang, C. Wang, J. Huang, C. Li, G. Qu, N. Li, S. Zhao, T. Li, D. Li, H. Qin and X. Xu, *Angew. Chem., Int. Ed.*, 2024, e202411884.
40 H. Cao, X. Zhang, B. Xie, X. Huang, F. Xie, Y. Huo, Q. Zheng, R. Zhao, Q. Hu, L. Kang, S. Liu and D. Lin, *Adv. Funct. Mater.*, 2023, **33**, 2305683.
41 Z. Wang, J. Diao, J. N. Burrow, K. K. Reimund, N. Katyal, G. Henkelman and C. B. Mullins, *Adv. Funct. Mater.*, 2023, **33**, 2304791.
42 Q. Meng, R. Zhao, P. Cao, Q. Bai, J. Tang, G. Liu, X. Zhou and J. Yang, *Chem. Eng. J.*, 2022, **447**, 137471.
43 J. Zheng, G. Tan, P. Shan, T. Liu, J. Hu, Y. Feng, L. Yang, M. Zhang, Z. Chen, Y. Lin, J. Lu, J. C. Neuefeind, Y. Ren, K. Amine, L.-W. Wang, K. Xu and F. Pan, *Chem*, 2018, **4**, 2872–2882.
44 R. Qin, Y. Wang, M. Zhang, Y. Wang, S. Ding, A. Song, H. Yi, L. Yang, Y. Song, Y. Cui, J. Liu, Z. Wang, S. Li, Q. Zhao and F. Pan, *Nano Energy*, 2021, **80**, 105478.
45 J. Zhou, H. Yuan, J. Li, W. Wei, Y. Li, J. Wang, L. Cheng, D. Zhang, Y. Ding, D. Chen and H. Wang, *Chem. Eng. J.*, 2022, **442**, 136218.
46 X. Li, J. Miao, F. Hu, K. Yan, L. Song, H. Fan, L. Ma and W. Wang, *J. Mater. Chem. A*, 2024, **12**, 968–978.
47 H. Zhang, Y. Zhong, J. Li, Y. Liao, J. Zeng, Y. Shen, L. Yuan, Z. Li and Y. Huang, *Adv. Energy Mater.*, 2023, **13**, 2203254.
48 G. Zhao, K. Rui, S. X. Dou and W. Sun, *Adv. Funct. Mater.*, 2018, **28**, 1803291.
49 M. Nezakat, H. Akhiani, S. M. Sabet and J. Szpunar, *Mater. Charact.*, 2017, **123**, 115–127.
50 D. Xu, B. Chen, X. Ren, C. Han, Z. Chang, A. Pan and H. Zhou, *Energy Environ. Sci.*, 2024, **17**, 642–654.
51 Q. Zong, B. Lv, C. Liu, Y. Yu, Q. Kang, D. Li, Z. Zhu, D. Tao, J. Zhang, J. Wang, Q. Zhang and G. Cao, *ACS Energy Lett.*, 2023, **8**, 2886–2896.